



## Research Article

# Hydrothermal synthesis of $K_3FeF_6$ and its electrochemical characterization as cathode material for lithium-ion batteries

Minqing Liu<sup>1</sup> · Yueli Shi<sup>1</sup>  · Quanchao Zhuang<sup>1</sup>

© Springer Nature Switzerland AG 2019

## Abstract

$K_3FeF_6$  was synthesized through a simple hydrothermal reaction for a novel cathode material of lithium-ion batteries. From the SEM and TEM images, the synthesized  $K_3FeF_6$  particles are about 30–50 nm after high energy ball milling.  $K_3FeF_6$  electrode delivers a high reversible capacity of 212.6 mAh g<sup>-1</sup> and it maintained 131 mAh g<sup>-1</sup> after 30 cycles. Additionally, in rate performance test, when the current density returns back to the 10 mA g<sup>-1</sup> again, the full recovery of the capacity exhibits its superior rate performance. The electrochemical redox mechanism, herein studied through Ex-situ XRD of  $K_3FeF_6$  electrodes at different polarization voltages, shows the satisfactory reversibility of structure.

**Keywords** Potassium iron fluoride · Cathode materials · Lithium-ion batteries · Electrochemical impedance spectroscopy

## 1 Introduction

Lithium ion batteries (LIBs) possess overwhelming advantages over other cell counterparts in developing reliable power sources. However, the limited capacity of conventional cathode materials, such as  $LiCoO_2$  (~140 mAh g<sup>-1</sup>) [1–4], can hardly meet the ever-growing demands. Moreover, sources of lithium and cobalt are relatively expensive. Thus, it is extremely urgent to explore cost-effective cathodes with readily available materials. For example, metal fluorides [5–8], oxides [9, 10], sulfides [11] and nitrides [12] have been explored for LIBs.

Fluorides as an intriguing candidate recently have attracted significant attention due to their high theoretical capacities, economical merits, low toxicity and good thermodynamic stability when used as cathodes in LIBs. Notably, fluorine shows high electronegativity. Therefore, the fluoride cathodes can deliver a high redox potential and operating voltage of as Li cells [13–16]. In fact, several

binary metal fluorides have been already reported for their high specific energies [8, 17–21], such as iron fluoride (712 mAh g<sup>-1</sup>, 1950 Wh kg<sup>-1</sup>) [22]. On the other hand, researches on ternary fluorides are intensified to facilitate the development of lithium-ion batteries. The Li-rich fluorides  $Li_2MnF_5$  and  $Li_3MF_6$  (M = V, Cr, Fe) concerning theoretical investigations have been published recently [13, 23–26]. And  $Li_3VF_6$  [27],  $LiMnF_4$  [28] and  $LiFe_2F_6$  [29] relating to electrochemical properties for Li cells have been reported as well.

Recently, it has been reported that  $Li_3FeF_6$  [26, 30–33] and  $Na_3FeF_6$  [34] electrodes for Li cells can deliver the reversible capacity up to ~100 mAh g<sup>-1</sup> and ~150 mAh g<sup>-1</sup>, respectively, after 20 cycles. Thus, it is particularly urgent to explore new metal fluorides so as to take advantage of their electrochemical characterization. Among the various ternary fluorides, the cubic  $K_3FeF_6$  in *Fm-3m* space group has a more symmetrical crystal structure, which means a more stable structure [35]. Meanwhile,  $K_3FeF_6$  electrode

**Electronic supplementary material** The online version of this article (<https://doi.org/10.1007/s42452-019-0904-7>) contains supplementary material, which is available to authorized users.

✉ Yueli Shi, [zwysyl@163.com](mailto:zwysyl@163.com); ✉ Quanchao Zhuang, [zhuangquanchao@126.com](mailto:zhuangquanchao@126.com) | <sup>1</sup>Lithium-ion Batteries Laboratory, School of Materials Science and Engineering, China University of Mining and Technology, Xuzhou 221116, China.



SN Applied Sciences (2019) 1:861 | <https://doi.org/10.1007/s42452-019-0904-7>

Received: 10 June 2019 / Accepted: 9 July 2019 / Published online: 15 July 2019

possesses a theoretical capacity of  $280 \text{ mAh g}^{-1}$ , which is much higher than the conventional cathodes ( $\text{LiCoO}_2$ ,  $\text{LiFePO}_4$ ,  $140\text{--}170 \text{ mAh g}^{-1}$ ).

$$C = \frac{N \times F}{3.6 \times M} \quad (1)$$

where  $C$  ( $\text{mAh g}^{-1}$ ) is specific capacity of a material,  $N$  represents the number of electrons transferred ( $N=3$ ),  $F$  is Faraday constant ( $96,485 \text{ C mol}^{-1}$ ),  $M$  ( $\text{g mol}^{-1}$ ) is the molecular weight of material, and the unit of factor 3.6 is  $\text{C mAh}^{-1}$ .

Herein, we have studied a concise solvothermal reaction to fabricate  $\text{K}_3\text{FeF}_6$  as a promising cathode material for LIBs. Thermogravimetric analysis (TGA) of  $\text{K}_3\text{FeF}_6$  exhibits only 0.3% weight loss when heated up to  $500^\circ\text{C}$ . Meanwhile, the electrochemical properties of  $\text{K}_3\text{FeF}_6$  electrode are also characterized and the electrochemical redox mechanism is checked by Ex-situ XRD.

## 2 Experimental

### 2.1 Preparation of the materials

$\text{K}_3\text{FeF}_6$  was fabricated via a solvothermal reaction as illustrated in Fig. 1. Briefly,  $\text{NH}_4\text{HF}_2$ ,  $\text{Fe}(\text{NO}_3)_3 \cdot 9\text{H}_2\text{O}$  and  $\text{KF}$  were dissolved in 8 mL distilled water to form a homogeneous solution, then adding 1 mL HF solution (40%) to the above

solution and stirring for 0.5 h at room temperature. Simultaneously, the mixed solution was poured into a sealed PTFE bottle, heating at  $180^\circ\text{C}$  for 72 h. Finally, the precipitation was collected by centrifugation and drying at  $60^\circ\text{C}$  for 12 h.

### 2.2 Characterization

The crystal structures of  $\text{K}_3\text{FeF}_6$  were investigated by  $\text{Cu K}\alpha$  radiation on a D/MAX-3B X-ray diffractometer. While, S-4800 and JEOL JEM-2010SEM were used to get scanning electron microscopy (SEM) images. The thermogravimetric analysis (TGA) data was recorded from room temperature up to  $500^\circ\text{C}$  under nitrogen atmosphere ( $10^\circ\text{C min}^{-1}$ ). X-ray spectroscopy (XPS) spectra were obtained to analyze the chemical bonds and elements of  $\text{K}_3\text{FeF}_6$ .

### 2.3 Electrochemical measurements

$\text{K}_3\text{FeF}_6$  electrode was prepared by spreading a mixture onto an aluminum foil, which were composed of 70 wt%  $\text{K}_3\text{FeF}_6$ , 20 wt% carbon black and 10 wt% PVDF binder. The electrolyte consisted of  $1 \text{ mol}\cdot\text{L}^{-1}$   $\text{LiPF}_6$  in a mixture of EC, DMC and DEC (wt%, 1:1:1). Charge–discharge test was carried out with CR2025-type coin cells. Cyclic voltammetry (CV,  $0.2 \text{ mV s}^{-1}$ ,  $1.0\text{--}4.5 \text{ V}$ ) and electrochemical impedance spectroscopy (EIS) was measured using an electrochemical workstation (CHI660D).

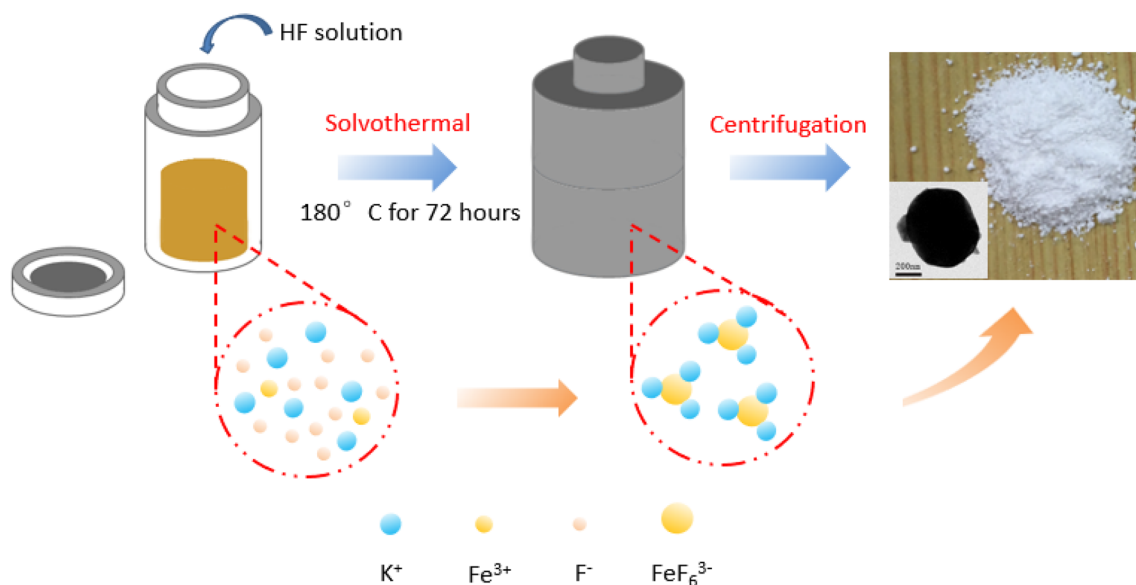


Fig. 1 Schematic of the synthetic process for  $\text{K}_3\text{FeF}_6$

## 3 Results and discussion

### 3.1 XRD analysis of synthesized material

The X-ray powder diffraction pattern of  $K_3FeF_6$  (Fig. 2a) match well with the standard data of  $K_3FeF_6$  (PDF#22-1223). According to XRD analysis, the synthesized  $K_3FeF_6$  possesses a cubic structure with space group  $Fm-3m$ . The Fe in  $K_3FeF_6$  crystal structure (Fig. 2b) is surrounded by six fluorine atoms in a regular octahedron. There are two potassium sites (K1, K2), which are located at the octahedral site of  $(KFe_6)$  and the tetrahedral site of  $(KFe_4)$  [35–37], respectively.

### 3.2 XPS and TGA tests

XPS measurements are carried out to analyse the  $K_3FeF_6$  chemical bonds, and F 1s, Fe 2p and K 2p spectra are shown in Fig. 3. The spectrum of F 1s has one peak (Fig. 3a), which is located at 684.01 eV, belonging to F–Fe bond [38–40]. The Fe 2p core level spectrum (Fig. 3b) shows two main peaks at 714.7 eV and 728.01 eV, indicating  $Fe^{3+}$  in  $K_3FeF_6$  [41–43], which are corresponded to Fe2p<sub>1/2</sub> and Fe2p<sub>3/2</sub>, respectively. Meanwhile, there are three diminutive peaks at 723.32 eV, 713.24 eV and 710.25 eV. The 723.32 eV peak can be attributed to the Fe–F bonds [44]. For the K2p spectrum (Fig. 3c), the peaks at 292.66 eV and 295.36 eV are corresponded to K2p<sub>3</sub> and K2p<sub>1</sub>, respectively. Through the above analysis, it is known that  $K_3FeF_6$  has been synthesized. TGA is conducted to investigate the thermal stability of  $K_3FeF_6$  (Fig. 3d), which exhibits only 0.3% weight loss when heated up to 500 °C. The  $K_3FeF_6$  weight loss only appears at about 200 °C, which is corresponding to the moisture evaporation from the material. Based on TGA

data, the synthesized material is very stable in term of high temperature (~500 °C).

### 3.3 SEM and TEM images of $K_3FeF_6$ powders

The different magnifications morphology of  $K_3FeF_6$  powders are studied by SEM and TEM.  $K_3FeF_6$  particles shows an irregular spherical shape with the size of about 200–300 nm (Fig. 4a–d). After high-energy ball milling (Fig. 4e, f), they are about 30–50 nm.

### 3.4 CV and charge–discharge test

CV curves (Fig. 5a) are given to study the  $K_3FeF_6$  electrode for Li cells (1.0–4.5 V, 0.2 mV s<sup>-1</sup>). In the initial lithiation process, there are two reversible peaks at 1.6 V (R1), and 1.4 V (R2). R1 and R2 are related to the conversion reaction step in Eq. (2) and (3) [34, 45], respectively.



Meanwhile, there are two consecutive oxidation peaks at around 2.5 V(O1) and 4.0 V(O2) in the delithiation process, O1 is ascribed to the reversible oxidation of  $Fe^0$  to  $Fe^{3+}$ , while O2 is corresponded to the decomposition of the electrolyte [46]. In addition, after 2 cycles, the well overlapped CV curves displays an excellent stability and superior reversibility of  $Li^+$  insertion/extraction in the subsequent cycles.

Figure 5b shows the large initial irreversible capacity which due to the formation of the SEI film on the active material surface and the decomposition of electrolyte [47, 48]. The decent reversible capacity (212.6 mAh g<sup>-1</sup>)  $K_3FeF_6$  electrode is superior to some of the reported fluorides in

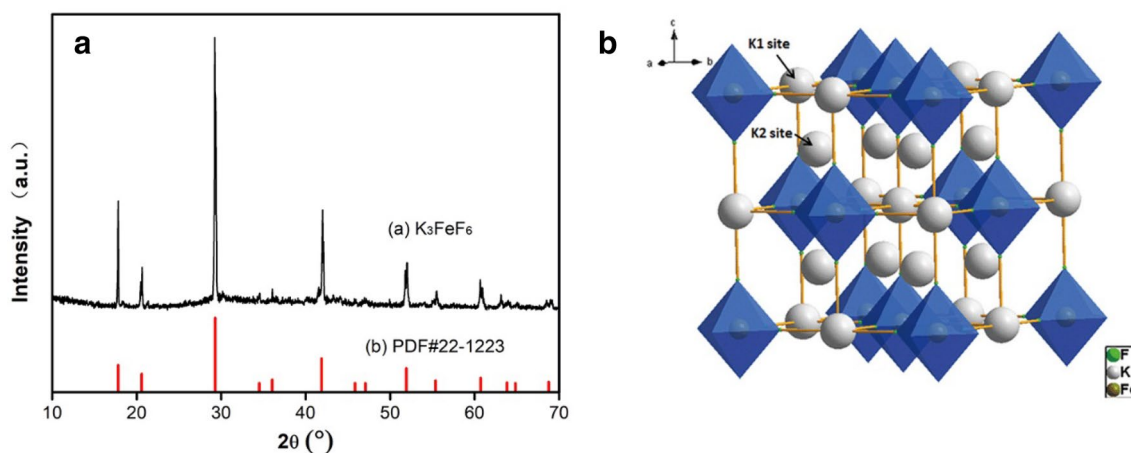
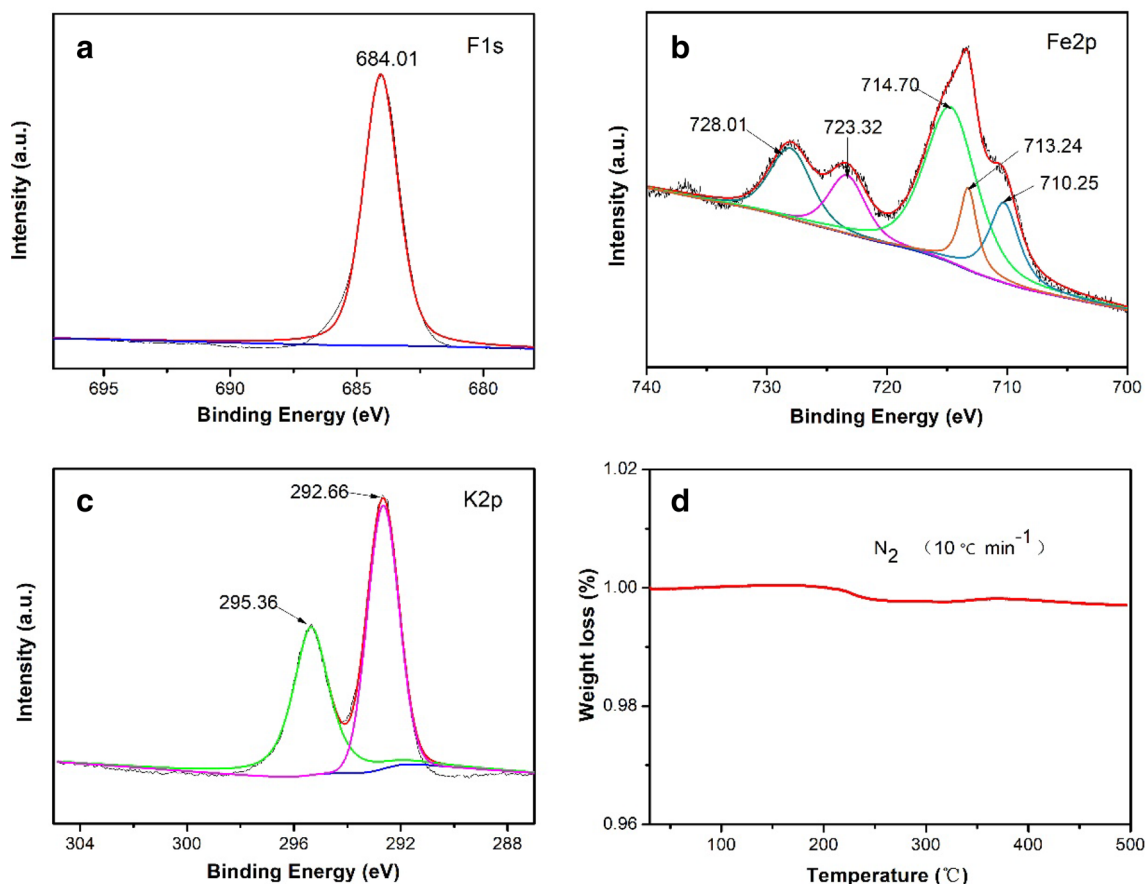


Fig. 2 The XRD patterns of  $K_3FeF_6$  (a) and schematic illustration of the  $K_3FeF_6$  structures (b)



**Fig. 3** XPS spectra of  $K_3FeF_6$  range from 0 to 1400 eV F 1s (a), Fe 2p (b), K 2p (c) and TGA curve (d) of  $K_3FeF_6$  in nitrogen when heated up to 500 °C

Li cells, showing in Tab.S1. Though the coulombic efficiency (CE) of the initial cycle is only 65.3%, it increases to 86.3% at the third cycle. Figure 5c shows the cycling data of  $K_3FeF_6$  electrode. After 30 cycles,  $K_3FeF_6$  electrode maintains 131 mA h  $g^{-1}$  (CE, 97.9%) with a capacity retention of 78.4% compared with the second cycle (167 mA h  $g^{-1}$ ). In rate performance test (Fig. 5d),  $K_3FeF_6$  electrode delivers the average reversible capacities of 145 (10 mA  $g^{-1}$ ), 92.3 (20 mA  $g^{-1}$ ), 53.7 (50 mA  $g^{-1}$ ) as well as 36.5 mA h  $g^{-1}$  (100 mA  $g^{-1}$ ), respectively. Notably, the discharge capacity of  $K_3FeF_6$  electrode can return to about 150 mA h  $g^{-1}$ , when the current density changes from 100 to 10 mA  $g^{-1}$ , implying the stable structure and superior reversibility of  $K_3FeF_6$  electrode.

### 3.5 XRD analysis of $K_3FeF_6$ electrodes at different voltages

Ex-situ XRD analysis was performed to explore the electrochemical redox mechanism of  $K_3FeF_6$  electrode (Fig. 6). In details, the typical peaks of  $K_3FeF_6$  can still be observed when discharging to 1.6 V and meanwhile new peaks at

38.7°, 45.0°, 65.5° appears, which is related to LiF (PDF#78-1217). When the potential decreases to 1.4 V, the typical peaks of  $K_3FeF_6$  are not very obvious and new peaks at 44.6° and 65° associated with  $Fe^0$  (PDF#06-0696) appears, suggesting that  $Fe^{3+}$  reduction to  $Fe^0$ . The peaks of LiF and  $Fe^0$  become sharper when discharged to 1.0 V, illustrating that more LiF and  $Fe^0$  generated. The results above are corresponding to the CV observations. In charging process, the typical peaks of  $K_3FeF_6$  become strong again when potential increases to 4.5 V. This phenomenon suggests the reversible reaction of  $K_3FeF_6$  with lithium-ions, indicating a superior reversibility and a stable structure of  $K_3FeF_6$  electrode.

### 3.6 EIS analysis of $K_3FeF_6$ electrodes

In Fig. 7, EIS is used to further investigate the electrochemical performances. At the open circuit voltage (3.42 V, Fig. 7a), the EIS curve of  $K_3FeF_6$  electrodes consisted of two parts: high-frequency semicircle (HFS) and low-frequency line (LFL), which is ascribed to the SEI film and solid-state diffusion, respectively [49, 50]. With the

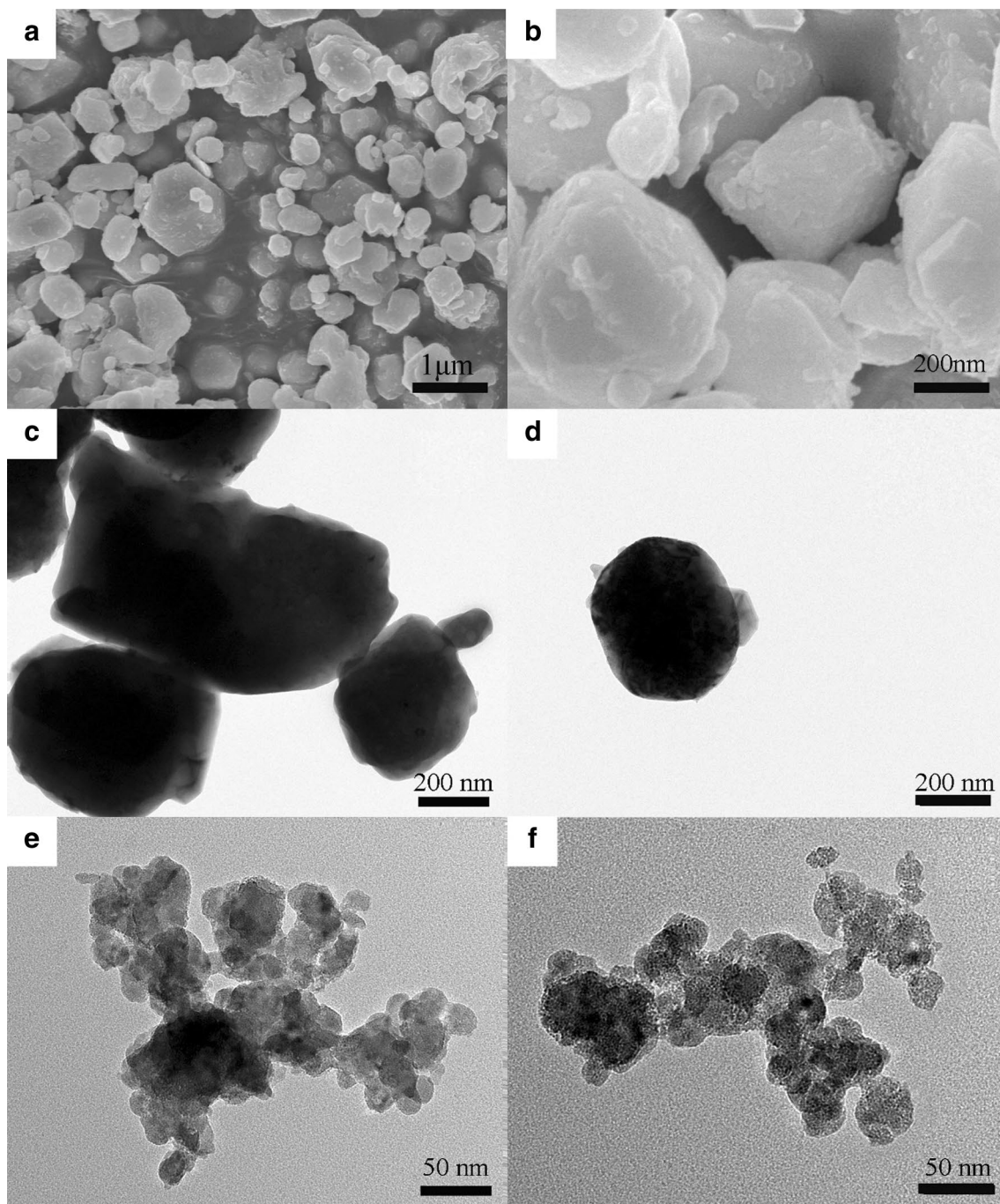


**Fig. 4** SEM images of  $K_3FeF_6$  (**a, b**); TEM images of  $K_3FeF_6$  before (**c, d**) and after (**e, f**) high energy ball milling

potential decrease, the small HFS increases and elongate at 1.6 V (Fig. 7b), then it turned into two semicircles and LFL converts into a large arc at 1.4 V (Fig. 7c). Therefore, the Nyquist graphs at 1.4 V are composed of three parts: HFS, middle-frequency semicircle (MFS) and low-frequency arc (LFA). With the electrode potential decreasing to 1.0 V (Fig. 7d), both HFS and MFS increase rapidly. When the potential further increase to 2.5 V (Fig. 7e),

an inclined line replaces the arc in the low frequency. Moreover, when charging to 4.0 V (Fig. 7f), both HFS and MFS become small. As shown in Figs. 1, S2, the Nyquist plots can consist of three parts: HFS, MFS and LFA/LFL, corresponding to lithium ion migration through the SEI film, the charge transfer resistance and lithium ions solid-state diffusion within the active electrode, respectively [51].

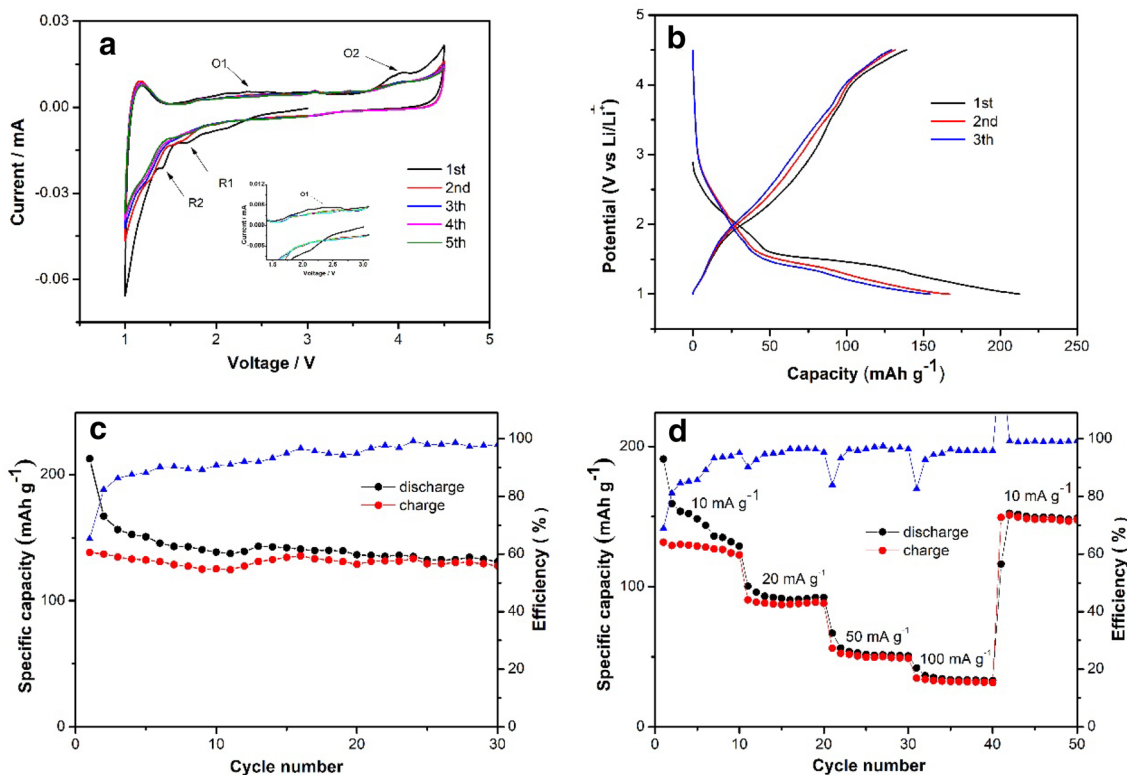


**Fig. 5** **a** CV curves ( $0.2 \text{ mV s}^{-1}$ ,  $1.0\text{--}4.5 \text{ V}$ ), **b** galvanostatic charge–discharge curves ( $10 \text{ mA g}^{-1}$ ), **c** cycling performance ( $10 \text{ mA g}^{-1}$ ) and **d** rate performance of  $\text{K}_3\text{FeF}_6$  electrodes

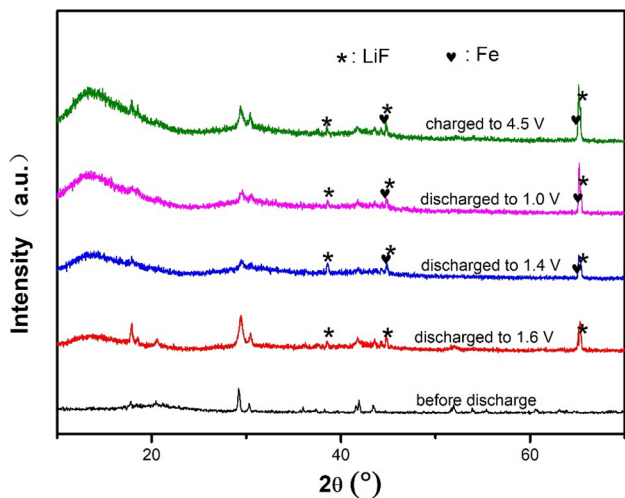


**Fig. 6** Ex-situ XRD analysis of  $\text{K}_3\text{FeF}_6$  in Li cells at different voltages of the first cycle

An equivalent circuit (Fig. 7g) is given to fit the EIS of  $\text{K}_3\text{FeF}_6$  electrode. In details,  $R_s$ ,  $R_1$  and  $R_2$  represent Ohmic resistance, resistance of SEI film and charge transfer resistance, respectively. Additionally,  $Q_1$  and  $Q_2$  are the constant phase elements (CPE). Figs. S3, S4 show the simulated EIS

compared with experimental EIS curves (discharge:  $1.4 \text{ V}$ , charge:  $2.8 \text{ V}$ ), and Table S2, S3 show the corresponding parameters of  $\text{K}_3\text{FeF}_6$  electrodes. In details, the uncertainties of all parameters are below 10%, suggesting that the equivalent circuit model can fit well with experimental data. Figure 8a provides the changes of  $R_1$  of  $\text{K}_3\text{FeF}_6$  electrode received from the fitting EIS data in the initial discharge–charge process. In the discharge process,  $R_1$  almost have no changes from  $3.4$  to  $1.4 \text{ V}$ . However, from  $1.4$  to  $1.0 \text{ V}$ , it grows swiftly. From the above experimental results (Figs. 5a, 6), LiF appears due to the conversion reactions at  $1.4 \text{ V}$ . According to the literature, LiF is one of the main components of SEI film. Thus, the growing up of HFS radius in the vicinity of reaction potential is ascribed to SEI film formation. In the initial charge process (Fig. 8a),  $R_1$  rises firstly and reaches the maximum at around  $2.6 \text{ V}$ , then it decreases rapidly after  $2.6 \text{ V}$ . This phenomenon mainly results from the reversible generating and decomposition of SEI film. Based on previous research, LiF generated in the conversion reactions is the composition of the SEI film, so insertion/extraction lithium-ion reaction should also affect the change of the SEI film.

Figure 8b shows the  $R_2$  changes of  $\text{K}_3\text{FeF}_6$  electrode in middle-frequency region in the initial discharge–charge process. From the open circuit potential ( $3.4 \text{ V}$ ) to  $1.6 \text{ V}$ ,

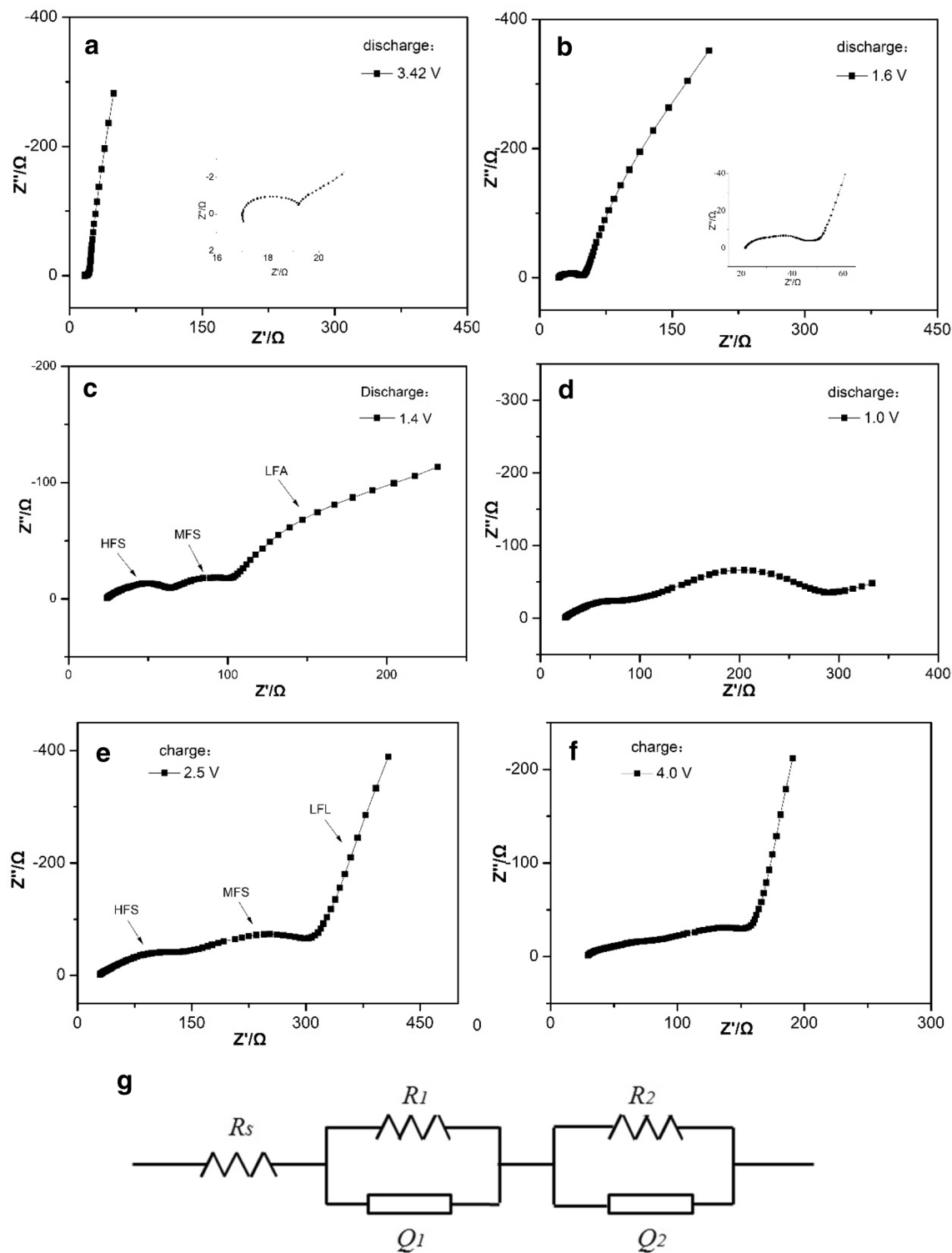


**Fig. 7** EIS experimental data of  $K_3FeF_6$  electrode at various potential 3.42 V (a), 1.6 V (b), 1.4 V (c), 1.0 V (d) at the first discharge process and 2.5 V (e), 4.0 V (f) at the first charge process and equivalent circuit proposed for analysis of the  $K_3FeF_6$  electrodes (g)

$R_2$  almost keeps stable. However, after 1.6 V,  $R_2$  begins to increase, originating from the first step conversion reaction ( $2K_3FeF_6 + Li \leftrightarrow LiF + 6KF + Fe_2F_7$ ). Then  $R_2$  shows swift growth after 1.3 V, which obviously is ascribed to the

Fe, LiF and KF generating in the discharge process. In the charge process,  $R_2$  firstly keeps growth (1.1–1.5 V) and then decreases (1.5–2.7 V), which shows a superior reversibility.

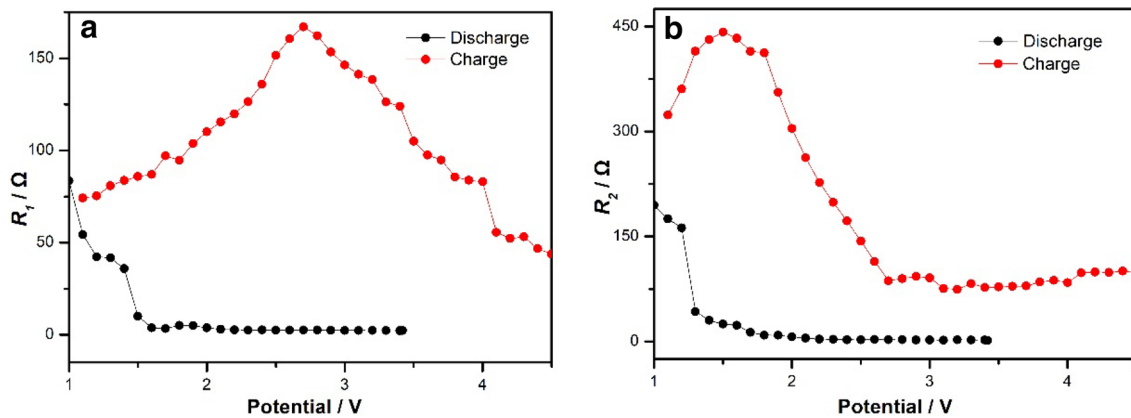


**Fig. 8** Variations of  $R_1$ (a) and  $R_2$ (b) of  $K_3FeF_6$  electrode with the electrode potential in the initial discharge–charge process

## 4 Conclusion

$K_3FeF_6$  was synthesized by a simple solvothermal method and applied to cathode materials for Li cells. TGA data exhibits only 0.3% weight loss ( $\sim 500\text{ }^\circ\text{C}$ ), implying the good thermal stability of  $K_3FeF_6$ . After high energy ball milling,  $K_3FeF_6$  particles decrease to 30–50 nm. The 1st and 30th discharge capacities ( $10\text{ mA g}^{-1}$ ) are  $212.6\text{ mA h g}^{-1}$  and  $131\text{ mA h g}^{-1}$ , respectively. In rate performance test, the average reversible capacities of first 10 cycles ( $10\text{ mA g}^{-1}$ ) is 145, when the current density changes back to  $10\text{ mA g}^{-1}$  again, the discharge capacities can return to about  $150\text{ mA h g}^{-1}$ , showing a superior rate performance. The electrochemical redox mechanism, investigated by Ex-situ XRD of  $K_3FeF_6$  electrodes at different discharge–charge voltages, shows the reversibility of the reaction and the stable structure. EIS results revealed that, the EIS of  $K_3FeF_6$  electrode consists of HFS, MFS and LFC/LFL, respectively, which coincides with the insertion/extraction reaction mechanism model.

**Acknowledgements** This work was supported by the Fundamental Research Funds for the China University of Mining and Technology (2017XKQY063).

## Compliance with ethical standards

**Conflict of interest** On behalf of all authors, the corresponding author states that there is no conflict of interest.

## References

- Kohler R et al (2009) Laser-assisted structuring and modification of  $LiCoO_2$  thin films. *Proc SPIE Int Soc Opt Eng* 7202(24):3605
- Marsh RA et al (2001) Li ion batteries for aerospace applications. *J Power Sources* 97(01):25–27
- Ueda A, Ohzuku T (1994) Solid-state redox reactions of  $LiNi_{(1/2)}Co_{(1/2)}O_2$  (R3-m) for 4 volt secondary lithium cells. *J Electrochem Soc* 141(8):2010–2014
- Padhi AK, Nanjundaswamy KS, Goodenough JB (1997) Phospho-olivines as positive-electrode materials for rechargeable lithium batteries. *J Electrochem Soc* 144(4):1188–1194
- Hua X et al (2014) Comprehensive Study of the  $CuF_2$  Conversion Reaction Mechanism in a Lithium Ion Battery. *J Phys Chem C* 118(28):15169–15184
- Yamakawa N, Jiang M, Grey CP (2009) Investigation of the conversion reaction mechanisms for binary copper(II) compounds by solid-state nmr spectroscopy and X-ray diffraction. *Chem Mater* 21(14):3162–3176
- Sun H et al (2017) Preparation of anhydrous iron fluoride with porous fusiform structure and its application for Li-ion batteries. *Microporous Mesoporous Mater* 253:10–17
- Subburaj T et al (2017) Titanium oxide nanofibers decorated nickel-rich cathodes as high performance electrodes in lithium ion batteries. *J Ind Eng Chem* 51:223–228
- Liu J et al (2018)  $CuCr_2O_4@rGO$  nanocomposites as high-performance cathode catalyst for rechargeable lithium–oxygen batteries. *Nano-Micro Lett* 10(2):22
- Zhang J et al (2014) Synthesis of  $Co_2SnO_4$  hollow cubes encapsulated in graphene as high capacity anode materials for lithium-ion batteries. *J Mater Chem A* 2(8):2728–2734
- Wang Q et al (2018) Reduced graphene oxide-wrapped  $FeS_2$  composite as anode for high-performance sodium-ion batteries. *Nano-Micro Lett* 10(2):30
- Sun C et al (2018) Stable and reversible lithium storage with high pseudocapacitance in GaN nanowires. *ACS Appl Mater Interfaces* 10(3):2574
- Basa A et al (2012) Reaching the full capacity of the electrode material  $Li_3FeF_6$  by decreasing the particle size to nanoscale. *J Power Sources* 197(8):260–266
- Wang X et al (2015) Carbon nanotube- $CoF_2$  multifunctional cathode for lithium ion batteries: effect of electrolyte on cycle stability. *Small* 11(38):5164–5173
- Chu Q et al (2013) Facile preparation of porous  $FeF_3$  nanospheres as cathode materials for rechargeable lithium-ion batteries. *J Power Sources* 236(16):188–191
- Dimov N et al (2013) Transition metal  $NaMF_3$  compounds as model systems for studying the feasibility of ternary Li–M–F and Na–M–F single phases as cathodes for lithium–ion and sodium–ion batteries. *Electrochim Acta* 110(6):214–220

17. Kim S et al (2017) Improved performance in FeF<sub>2</sub> conversion cathodes through use of a conductive 3D scaffold and Al<sub>2</sub>O<sub>3</sub> ALD coating. *Adv Funct Mater* 27(35):1702783
18. Wei S et al (2016) The FeF<sub>3</sub>·0.33H<sub>2</sub>O/C nanocomposite with open mesoporous structure as high-capacity cathode material for lithium/sodium ion batteries. *J Alloys Compd* 689:945–951
19. Tawa S et al (2016) Iron(III) fluoride synthesized by a fluorolysis method and its electrochemical properties as a positive electrode material for lithium secondary batteries. *J Fluor Chem* 184:75–81
20. Guan Q et al (2016) Porous CoF<sub>2</sub> spheres synthesized by a one-pot solvothermal method as high capacity cathode materials for lithium-ion batteries. *Chin J Chem* 35(1):48–54
21. Groult H et al (2017) Nano-CoF<sub>3</sub> prepared by direct fluorination with F<sub>2</sub> gas: application as electrode material in Li-ion battery. *J Fluor Chem* 196:117–127
22. Li C et al (2010) Low-temperature ionic-liquid-based synthesis of nanostructured iron-based fluoride cathodes for lithium batteries. *Adv Mater* 22(33):3650–3654
23. Kohl J et al (2012) Synthesis of ternary transition metal fluorides Li<sub>3</sub>MF<sub>6</sub> via a sol–gel route as candidates for cathode materials in lithium-ion batteries. *J Mater Chem* 22(31):15819–15827
24. Melanie S et al (2013) Li<sub>x</sub>FeF<sub>6</sub> (x = 2, 3, 4) battery materials: structural, electronic and lithium diffusion properties. *Phys Chem Chem Phys* 15(47):20473–20479
25. Lieser G et al (2015) Electrochemical characterization of monoclinic and orthorhombic Li<sub>3</sub>CrF<sub>6</sub> as positive electrodes in lithium-ion batteries synthesized by a sol–gel process with environmentally benign chemicals. *J Power Sources* 294:444–451
26. Shi Y et al (2016) Enhanced charge storage of Li<sub>3</sub>FeF<sub>6</sub> with carbon nanotubes for lithium-ion batteries. *RSC Adv* 6(114):61–66
27. Basa A et al (2012) Facile synthesis of β-Li<sub>3</sub>VF<sub>6</sub>: A new electrochemically active lithium insertion material. *J Power Sources* 207:160–165
28. Twu N et al (2013) Synthesis and lithiation paths of dirutile and rutile LiMnF<sub>4</sub>: two new conversion cathode materials. *The Electrochemical Society*
29. Conte DE, Pinna N (2014) A review on the application of iron(III) fluorides as positive electrodes for secondary cells. *Mater Renew Sustain Energy* 3(4):37
30. Gonzalo E, Kuhn A, García-Alvarado F (2010) On the room temperature synthesis of monoclinic Li<sub>3</sub>FeF<sub>6</sub>: a new cathode material for rechargeable lithium batteries. *J Power Sources* 195(15):4990–4996
31. Lieser G et al (2014) Sol–gel processing and electrochemical characterization of monoclinic Li<sub>3</sub>FeF<sub>6</sub>. *J Sol–Gel Sci Technol* 71(1):50–59
32. Basa A et al (2011) On the electrochemical properties of α-Li<sub>3</sub>FeF<sub>6</sub> prepared by precipitation from aqueous-alcohol based solutions. In: MRS online proceedings library archive, vol 1313
33. Gonzalo E et al (2013) Defect and dopant properties of the α- and β-polymorphs of the Li<sub>3</sub>FeF<sub>6</sub> lithium battery material. *J Mater Chem A* 1(22):6588–6592
34. Shakoor RA et al (2012) Mechanochemical synthesis and electrochemical behavior of Na<sub>3</sub>FeF<sub>6</sub> in sodium and lithium batteries. *Solid State Ionics* 218(12):35–40
35. Allen GC, El-Sharkawy GAM, Warren KD (1971) Electronic spectra of the hexafluorometalate(III) complexes of the first transition series. *Inorg Chem* 10(11):2538–2546
36. Christoe CW, Drickamer HG (1969) Effect of pressure on the quadrupole interaction in iron-fluorine compounds. *Phys Rev B-Condens Matter* 1(4):1813–1822
37. Wiegardt K, Weiss J (2010) Die Kristallstrukturen von Hexamminchrom(III)-Hexafluoromanganat(III) und Hexamminchrom(III)-Hexafluoroferrat(III). *Acta Crystallogr A* 28(2):529–534
38. Feng W et al (2011) Conversion reaction mechanisms in lithium ion batteries: study of the binary metal fluoride electrodes. *J Am Chem Soc* 133(46):18828–18836
39. Hamwi A et al (1996) Perfluorofullerenes: characterization and structural aspects. *J Phys Chem Solids* 57(57):991–998
40. Bondarenka V et al (2015) XPS and optical properties of sol-gel processed vanadium pentoxide films. *Lith J Phys* 48(4):341
41. Gmitter AJ et al (2010) Formation, dynamics, and implication of solid electrolyte interphase in high voltage reversible conversion fluoride nanocomposites. *J Mater Chem* 20(20):4149
42. Pohl A et al (2016) Development of a water based process for stable conversion cathodes on the basis of FeF<sub>3</sub>. *J Power Sources* 313:213–222
43. Frederic C et al (2007) EELS spectroscopy of iron fluorides and FeF<sub>x</sub>/C nanocomposite electrodes used in Li-ion batteries. *Microsc Microanal* 13(2):87–95
44. Yang J et al (2017) A cathode material based on the iron fluoride with an ultra-thin Li<sub>3</sub>FeF<sub>6</sub> protective layer for high-capacity Li-ion batteries. *J Power Sources* 363:244–250
45. Mestre-Aizpurua F et al (2010) High temperature lithium cells using conversion oxide electrodes. *J Appl Electrochem* 40(7):1365–1370
46. Li L et al (2017) In situ engineering toward core regions: a smart way to make applicable FeF<sub>3</sub>@carbon nanoreactor cathodes for li-ion batteries. *ACS Appl Mater Interfaces* 9(21):17992–18000
47. Chun J et al (2016) Ammonium fluoride mediated synthesis of anhydrous metal fluoride-mesoporous carbon nanocomposites for high-performance lithium ion battery cathodes. *ACS Appl Mater Interfaces* 8(51):35180–35190
48. Wu C et al (2014) Synthesis and characterization of Fe@Fe<sub>2</sub>O<sub>3</sub> core-shell nanoparticles/graphene anode material for lithium-ion batteries. *Electrochim Acta* 134(5):18–27
49. Holzapfel M et al (2003) First lithiation and charge/discharge cycles of graphite materials, investigated by electrochemical impedance spectroscopy. *J Electroanal Chem* 546(1):41–50
50. Wang C, Appleby AJ, Little FE (2002) Electrochemical impedance study of initial lithium ion intercalation into graphite powders. *Electrochim Acta* 46(12):1793–1813
51. Aurbach D (2000) Review of selected electrode–solution interactions which determine the performance of Li and Li ion batteries. *J Power Sources* 89(2):206–218

**Publisher's Note** Springer Nature remains neutral with regard to jurisdictional claims in published maps and institutional affiliations.